Nuclear Science and Techniques (2025) 36:206
https://doi.org/10.1007/s41365-025-01777-2

Theoretical prediction of KF-RbF-CsF-BeF_2 system: phase diagrams calculation and ab initio molecular dynamics

Hui-Qin Yin[1] · Lin-Bing Jiang[1] · Xuan-Chun Wu[1] · Biao Hu[3] · Yang Wang[2] · Wen-Guan Liu[1]

Received: 2 July 2024 / Revised: 18 October 2024 / Accepted: 28 November 2024 / Published online: 14 August 2025

Abstract

Thermodynamic optimization of the AF-BeF_2 (A = K, Rb, and Cs), KF-CsF, and RbF-CsF systems was performed within the framework of phase diagrams calculation. The model parameters were optimized based on experimental data and theoretically calculated values. The results show that the thermodynamically calculated values for the AF-BeF_2 (A = K, Rb, and Cs), KF-CsF, and RbF-CsF systems agree well with the experimental data. Next, a set of reliable and self-consistent thermodynamic databases was built, and the liquidus projections and invariant points of the sub-ternary systems of the KF-RbF-CsF-BeF_2 system were calculated. Furthermore, the melting temperature with the corresponding composition was predicted using the phase diagrams calculation technique, and the radial distribution functions, coordination numbers, angular distribution functions, and diffusion coefficients of the quaternary KF-RbF-CsF-BeF_2 system were calculated using ab initio molecular dynamics. The results show that the quaternary KF-RbF-CsF-BeF_2 system with the proportion 3.50–28.92–21.78–45.80 mol% or 1.80–35.42–52.40–10.38 mol% is one of the most promising candidate coolants for molten salt reactors in terms of thermodynamics and kinetics. This work provides direct guidelines for the screening and optimization of molten salts in the nuclear energy field.

Keywords Molten salt · KF-RbF-CsF-BeF_2 · Calculation of phase diagrams · Ab initio molecular dynamics

1 Introduction

Molten salt reactors (MSRs) are the only liquid fuel reactors among the Generation IV nuclear reactors, where the fissile and fertile fluorides (i.e., UF_4, ThF_4, and PuF_3) are dissolved into the molten fluoride salt [1–3]. MSRs have received increasing attention worldwide owing to their significant advantages, such as good neutron economy, less nuclear waste, no water cooling, online post-processing of fission products, and low pressure at high temperature [4–8]. Molten fluoride salt is used as a nuclear fuel and heat transfer fluid medium because of its good neutron properties and excellent thermophysical properties, which play a critical role in the design of nuclear cores, thermal hydraulic calculations, nuclear reactor safety analysis, and the entire operation of nuclear reactors [9–13]. Relevant fluoride salts, which are essential for the design, research, and development of heat transfer media for MSRs must be explored thoroughly.

Molten BeF_2-based salt is considered one of the most promising heat transfer media and nuclear fuel salt carriers

This work was supported by the National Natural Science Foundation of China (Nos. 12205364 and 12375282), Guangdong Provincial Natural Science Foundation (Nos. 2024A1515012570 and 2024A1515010885), and the Fundamental Research funds for the Central Universities, Sun Yat sen University.

✉ Yang Wang
wangyang@sinap.ac.cn

✉ Wen-Guan Liu
liuwg7@mail.sysu.edu.cn

[1] Sino-French Institute of Nuclear Engineering and Technology, Sun Yat-Sen University, Zhuhai 519082, China

[2] Shanghai Institute of Applied Physics, Chinese Academy of Sciences, Shanghai 201800, China

[3] School of Materials Science and Engineering, Anhui University of Science and Technology, Huainan 232001, Anhui, China

for MSRs due to its favorable thermal neutron-capture cross-section (< 1 barn) and thermophysical properties [14–17]. LiF-BeF_2 is the classic coolant and nuclear fuel medium for the MSRs at Shanghai Institute of Applied Physics in China [18] and Oak Ridge National Laboratory (ORNL) in the U.S. [19]. The LiF-BeF_2 system has been extensively investigated by many researchers. The phase diagram information of the LiF-BeF_2 system was first determined through thermal analysis and thermal gradient quenching by Roy et al. [20], and Moore et al. [21]. Later, the liquidus of the LiF-BeF_2 phase diagram with a 0.12–0.58 mol fraction of BeF_2 was again measured through the electromotive force method by Romberger et al. [22]. The thermochemical properties (i.e., the activity coefficient [23] and mixing enthalpy of the liquid phase [24]) of the LiF-BeF_2 system were experimentally investigated using the electromotive force and single-unit microcalorimeter methods, respectively. The LiF-BeF_2 system was first optimized using Redlich–Kister polynomials by Meer et al. [25], and the thermophysical properties (i.e., the melting point [26], specific heat capacity [17, 27], density [17, 28], viscosity [28–31], vapor pressure [32], thermal conductivity [10], and local structure [33–36]) have been thoroughly studied by performing experimental measurements and theoretical calculations. Compared with the LiF-BeF_2 system, the NaF-BeF_2 system has not been reported on as thoroughly. The phase diagram of the NaF-BeF_2 system was measured based on the differential thermal analysis techniques, high-temperature X-ray diffraction, and the quenching method by Roy et al. [37]. The thermodynamic database of the NaF-BeF_2 system was later built based on the substitutional solution model by Wu et al. [38]. Only limited experimental data regarding the properties of NaF-BeF_2 (i.e., the melting point [10], density [39], viscosity [39], specific heat capacity [17], vapor pressure [40], activity coefficient [41], and local structure [42]) have been reported. The thermophysical properties of the NaF-BeF_2 system were solely calculated using first-principles molecular dynamics by Liu et al. [43]. For the KF-BeF_2 system, limited thermodynamic property information has been obtained [17, 21, 44, 45]. Only the phase equilibria information [21, 46] and a few thermophysical properties [39] for the RbF-BeF_2 system have been experimentally determined, and only the experimental phase diagram of the CsF-BeF_2 system has been determined by thermal analysis [47]. Until now, little other experimental or theoretical information about the AF-BeF_2 (A = K, Rb, and Cs) system has been available, although this information is foundational for the design and operation of processes utilizing molten fluoride salts. Studying the thermodynamic characteristics of the AF-BeF_2 (A = K, Rb, and Cs) system only through experimental measurements is also challenging owing to the difficulty and uncertainty of high-temperature experiments with highly toxic BeF_2. Calculation of phase diagrams (CALPHAD) is one of the most effective techniques for studying the phase equilibria behavior of multi-component systems based on minimal experimental data. Due to its high accuracy and universality, ab initio molecular dynamics (AIMD) is a powerful tool for investigating the interionic forces, local structures, and physio-chemical properties of multi-component systems and has been successfully applied to the LiF-BeF_2 [48–50], NaF-BeF_2 [43, 51], and KF-NaF-AlF_3 [52] systems, among others. In the present work, phase diagrams calculations and AIMD were employed to investigate the thermodynamic and kinetics characteristics of the quaternary KF-RbF-CsF-BeF_2 system.

The thermodynamic calculations for the KF-BeF_2, RbF-BeF_2, CsF-BeF_2, KF-CsF, and RbF-CsF systems were performed using the CALPHAD technique based on experimental data and theoretically calculated values. A substitutional solution model was used to depict the liquid and solid solution phases, and compound energy formalism was employed to describe the intermediate phases, i.e., $ABeF_3$, A_2BeF_4, A_3BeF_5, and ABe_2F_5 (A = K, Rb, and Cs). The results showed that the thermodynamically calculated values for the KF-BeF_2, RbF-BeF_2, CsF-BeF_2, KF-CsF, and RbF-CsF systems agreed well with the experimental data. Finally, a set of self-consistent and reliable thermodynamic databases was obtained. Additionally, the liquidus projection and invariant points of the corresponding ternary systems of the KF-RbF-CsF-BeF_2 system were calculated. Furthermore, the melting temperatures with the corresponding compositions, radial distribution functions (RDFs), coordination numbers (CNs), angular distribution functions (ADFs), and diffusion coefficients of the quaternary KF-RbF-CsF-BeF_2 system were calculated using AIMD. The results showed that the quaternary KF-RbF-CsF-BeF_2 (3.50–28.92–21.78–45.80 mol% or 1.80–35.42–52.40–10.38 mol%) system is one of the most promising candidate coolants for MSRs in terms of thermodynamics and kinetics. The thermodynamic parameters of the KF-BeF_2, RbF-BeF_2, CsF-BeF_2, KF-CsF, and RbF-CsF systems were firstly built using the CALPHAD technique. The kinetic characteristics of the quaternary KF-RbF-CsF-BeF_2 (3.50–28.92–21.78–45.80 mol% or 1.80–35.42–52.40–10.38 mol%) system were also first obtained in this study using AIMD. These are important fundamentals for thoroughly exploring heat transfer media and nuclear fuel carriers for MSRs. This work provides guidelines for the screening and optimization of molten salts in the nuclear energy field.

2 Literature evaluation

2.1 KF-BeF_2 system

The phase equilibrium information of the KF-BeF_2 system has been reported by three groups of investigators using thermal analysis. The experimental phase diagram of the KF-BeF_2 system was first established by Borzenkova et al. [44]. Four intermediate phases—K_3BeF_5, K_2BeF_4, $KBeF_3$, and KBe_2F_5—were detected in the KF-BeF_2 system, where only three compounds—K_3BeF_5, K_2BeF_4, and $KBeF_3$—were stable from room temperature to the melting temperature, whereas KBe_2F_5 was decomposed into $KBeF_3$ and BeF_2 at 278.0 °C. Afterwards, the KF-BeF_2 system was experimentally determined by Moore et al. [21] at ORNL. The four compounds were again discovered, where K_3BeF_5, K_2BeF_4, and KBe_2F_5 were melted congruently at 740.0 °C, 787.0 °C and 353.0 °C, whereas $KBeF_3$ was melted incongruently at 405.5 °C; these findings are substantially different from those of Borzenkova et al. [44]. Thus, four eutectic reactions ($\text{Liquid} \xrightarrow{720.0\,^{\circ}C} KF + K_3BeF_5$, $\text{Liquid} \xrightarrow{730.0\,^{\circ}C} K_3BeF_5 + K_2BeF_4$, $\text{Liquid} \xrightarrow{330.0\,^{\circ}C} KBeF_3 + KBe_2F_5$, and $\text{Liquid} \xrightarrow{323.0\,^{\circ}C} KBe_2F_5 + BeF_2$) and one peritectic reaction ($\text{Liquid} + K_2BeF_4 \xrightarrow{390.0\,^{\circ}C} KBeF_3$) occurred in the KF-$BeF_2$ system. Novoselova et al. [45] later measured the phase diagram of the KF-BeF_2 system, determining that K_3BeF_5 was incongruently melted at 740.0 °C with a peritectic composition of 0.25 mol BeF_2. Naturally, the KF-BeF_2 system reported by Novoselova et al. is characterized by three eutectic reactions ($\text{Liquid} \xrightarrow{700.0\,^{\circ}C} KF + K_3BeF_5$, $\text{Liquid} \xrightarrow{327.0\,^{\circ}C} KBeF_3 + KBe_2F_5$, and $\text{Liquid} \xrightarrow{346.0\,^{\circ}C} KBe_2F_5 + BeF_2$) and two peritectic reactions ($\text{Liquid} + K_2BeF_4 \xrightarrow{740.3\,^{\circ}C} K_3BeF_5$ and $\text{Liquid} + K_2BeF_4 \xrightarrow{405.5\,^{\circ}C} KBeF_3$). To date, thermochemical data and thermodynamic parameters for the KF-BeF_2 system are still rare. Herein, the KF-BeF_2 system was thermodynamically optimized through the substitutional solution model in terms of the relatively accurate experimental data from Moore et al. [21].

2.2 RbF-BeF_2 system

A phase diagram of the RbF-BeF_2 system was constructed by two groups of investigators using thermal analysis. Grebenshchikov [46] first established the entire phase diagram of the RbF-BeF_2 system, in which four intermediate phases—Rb_2BeF_4, $Rb_3Be_2F_7$, $RbBeF_3$ and $RbBe_2F_5$—were detected. Three compounds—Rb_2BeF_4, $RbBeF_3$, and $RbBe_2F_5$—were stable and congruently melted separately at 792.0 °C, 464.0 °C, and 451.0 °C, whereas $Rb_3Be_2F_7$ was unstable and decomposed to Rb_2BeF_4 and $RbBeF_3$ when the temperature was higher than 423.5 °C. In addition, Rb_2BeF_4 and $RbBe_2F_5$ are not simple stoichiometric compounds and have a certain solid solubility. Eventually, four eutectic reactions ($\text{Liquid} \xrightarrow{689.0\,^{\circ}C} RbF + Rb_2BeF_4$, $\text{Liquid} \xrightarrow{461.0\,^{\circ}C} Rb_2BeF_4 + RbBeF_3$, $\text{Liquid} \xrightarrow{394.0\,^{\circ}C} RbBeF_3 + RbBe_2F_5$, and $\text{Liquid} \xrightarrow{424.0\,^{\circ}C} RbBe_2F_5 + BeF_2$) were formed for the RbF-BeF_2 system. Subsequently, Moore et al. [21] reported the phase equilibrium information of the RbF-BeF_2 system and discovered four intermediate phases: Rb_3BeF_5, Rb_2BeF_4, $RbBeF_3$, and $RbBe_2F_5$. The presence of Rb_3BeF_5 versus $Rb_3Be_2F_7$ was the biggest difference between the works of Grebenshchikov and Moore et al. Moreover, the intermediate compounds Rb_3BeF_5, Rb_2BeF_4, and $RbBe_2F_5$ melted congruently, whereas $RbBeF_3$ melted incongruently. Consequently, four eutectic reactions ($\text{Liquid} \xrightarrow{675.0\,^{\circ}C} RbF + Rb_3BeF_5$, $\text{Liquid} \xrightarrow{720.0\,^{\circ}C} Rb_2BeF_4 + Rb_3BeF_5$, $\text{Liquid} \xrightarrow{383.0\,^{\circ}C} RbBeF_3 + RbBe_2F_5$, and $\text{Liquid} \xrightarrow{397.0\,^{\circ}C} RbBeF_3 + BeF_2$) and one peritectic reaction ($\text{Liquid} + Rb_2BeF_4 \xrightarrow{442.0\,^{\circ}C} Rb_3BeF_5$) were observed in the RbF-BeF_2 system. Little thermochemical information about the RbF-BeF_2 system has been reported to date. The RbF-BeF_2 system was optimized in this study based on the substitutional solution model using the experimental data from Moore et al. [21], because their data were more accurate than those of Grebenshchikov [46].

2.3 CsF-BeF_2 system

Only Breusov et al. [47] reported the phase equilibrium information of the CsF-BeF_2 system using thermal analysis. The CsF-BeF_2 system contains four intermediate compounds—Cs_3BeF_5, Cs_2BeF_4, $CsBeF_3$ and $CsBe_2F_5$—where Cs_2BeF_4, $CsBeF_3$, and $CsBe_2F_5$ were discovered to melt congruently at 793.0 °C, 475.0 °C, and 480.0 °C, respectively, but Cs_3BeF_5 melted incongruently at 659.0 °C. Four eutectic reactions ($\text{Liquid} \xrightarrow{598.0\,^{\circ}C} CsF + Cs_3BeF_5$, $\text{Liquid} \xrightarrow{449.0\,^{\circ}C} Cs_2BeF_4 + CsBeF_3$, $\text{Liquid} \xrightarrow{393.0\,^{\circ}C} CsBeF_3 + CsBe_2F_5$, and $\text{Liquid} \xrightarrow{367.0\,^{\circ}C} CsBe_2F_5 + BeF_2$) and one peritectic reaction ($\text{Liquid} + Cs_2BeF_4 \xrightarrow{659.0\,^{\circ}C} Cs_3BeF_5$) were the distinct features of the CsF-BeF_2 system. Thermochemical data for the CsF-BeF_2 system are still lacking. Similar to the systems mentioned above, a substitutional solution model was used to optimize this system based on experimental data from Breusov et al. [41].

2.4 KF-CsF system

The phase diagram of the KF-CsF system was solely obtained by Samuseva et al. [53] through thermal analysis. This system is eutectic with one eutectic point located at 625.0 °C and 0.570 mol CsF. In addition, the limited solid solubility of KF in CsF is 0.15 mol at 625.0 °C. To date, few thermochemical studies of the KF-CsF system have been reported. A substitutional solution model was used to optimize the KF-CsF system based on experimental data from Samuseva et al. [53].

2.5 RbF-CsF system

The phase diagram of the RbF-CsF system was investigated by Samuseva et al. [53] and Beneš et al. [54] using thermal analysis. The phase diagram reported by Samuseva et al. [53] shows a temperature minimum for the solidus without a corresponding minimum for the liquidus, which violates the phase rule. The liquidus of the RbF-CsF system was optimized by Sangster and Pelton [55] based on the liquidus experimental data of Samuseva et al. However, there was a significant deviation between the calculated phase diagram and liquidus experimental data obtained by Samuseva et al.

Subsequently, new measurements of the solidus and liquidus equilibria of the RbF-CsF system were obtained by Beneš et al. [54]. The phase diagram of the RbF-CsF system was first constructed using a quasi-chemical model based on the measured experimental data, where the calculated phase diagram agreed well with the experimental values. In this study, the RbF-CsF system was calculated using the substitutional solution model to maintain the consistency of the model. The experimental data from Beneš et al. were used to optimize the RbF-CsF system in the present work.

2.6 KF-RbF system

The KF-RbF system is isomorphous with a minimum point in the liquidus curve, which was systematically evaluated and optimized by Yin et al. [56]. The thermodynamic parameters obtained in that study were directly adopted in the present work.

2.7 Sub-ternary systems

Little relevant information has been reported to date for the ternary KF-RbF-BeF_2, KF-CsF-BeF_2, RbF-CsF-BeF_2, and KF-RbF-CsF systems. These ternary systems were investigated in this study based on the thermodynamic parameters of the binary systems using model extrapolation.

3 Methods

3.1 Thermodynamic optimization

The PanOptimizer module included in the PANDAT software, which is a C/C++ software package for optimizing thermodynamics and thermophysical properties, was used to optimize the thermodynamic parameters. The weighted least-squares technique was adopted during the optimization process, and a trial-and-error method was used to regulate the optimization weight factor until the optimized value agreed well with the experimental phase equilibrium data and the theoretically calculated value.

Table 1 Thermodynamic parameters of the KF-RbF-CsF-BeF_2 system from FactSage 7.2

Compound	Gibbs energy (J)	Temp. (K)
KF (Solid)	$-581{,}701.002+245.661\,T-45.982\ln(T)-0.007T^2$	298.15–2000
KF (Liquid)	$-567{,}937.997+372.694\,T-66.944T\ln(T)$	298.15–2000
RbF (Solid)	$-563{,}090.817+158.256\,T-33.330T\ln(T)-0.019T^2-251{,}040.000\,T^{-1}$	298.15–1500
	$-558{,}571.051+313.921\,T-58.994T\ln(T)$	1500–1663
RbF (Liquid)	$-546{,}097.480+300.480\,T-58.994T\ln(T)$	298.15–1066
	$-297{,}259.229-607.417\,T+47.292T\ln(T)-0.002T^2-73{,}360{,}164.000\,T^{-1}$	1066–1200
	$-544{,}409.532+298.957\,T-58.994T\ln(T)$	1200–1663
CsF (Solid)	$-569{,}380.712+229.686\,T-46.685T\ln(T)-0.009T^2$	298.15–2000
CsF (Liquid)	$-565{,}929.140+405.902\,T-74.057T\ln(T)$	298.15–2000
BeF_2 (Solid)	$-1{,}041{,}405.769+271.945\,T-47.363T\ln(T)-0.017T^2$	298.15–1300
	$-1{,}029{,}550.268+331.677\,T-60.000T\ln(T)$	1300–1301
BeF_2 (Liquid)	$-848{,}170.113-1703.462\,T+188.684T\ln(T)-1{,}415{,}912.346\,T^{-1}-5.801T^{1.5}+26{,}373.417T^{0.5}-74{,}606.149\ln(T)$	298.15–2000
	$-990{,}282.352+304.240\,T-60.000T\ln(T)-0.010T^2$	2000–2001

3.2 Thermodynamic model

3.2.1 Pure component

The Gibbs energy function of the pure component is described as follows, and the corresponding coefficients of the pure component are listed in Table 1:

$$^{\circ}G_i^{\phi}(T) = a + bT + cT\ln(T) + dT^2 + eT^3 + \frac{f}{T} + \sum_n g_n T^n \tag{1}$$

where *a–f* and g_n denote the corresponding coefficients, *n* refers to a set of integers, and *T* is the absolute temperature (K). The Gibbs free energy function of the pure components was adopted from the FactSage database.

3.2.2 Solution phase

The solution phase, that is, the liquid phase of the AF-BeF_2 (A = K, Rb, and Cs) and A′F-CsF (A′ = K and Rb) systems, and the solid solution phase of the A′F-CsF (A′ = K and Rb) system, were thermodynamically described using the substitutional solution model, where the Gibbs free energy is expressed as follows:

$$G^{\text{Liquid}}_{\text{AF - BeF}_2} = x_{\text{AF}}G^{\text{liq}}_{\text{AF}} + x_{\text{BeF}_2}G^{\text{liq}}_{\text{BeF}_2} + RT(x_{\text{AF}}\ln x_{\text{AF}} + x_{\text{BeF}_2}\ln x_{\text{BeF}_2}) + x_{\text{AF}}x^{\upsilon}_{\text{BeF}_2}L^{\text{liq}}_{x_{\text{AF}},x_{\text{BeF}_2}}(x_{\text{AF}} - x_{\text{BeF}_2})^{\upsilon} \quad (\text{A} = \text{K, Rb and Cs}) \tag{2}$$

$$G^{\text{Liquid}}_{\text{A′F–CsF}} = x_{\text{A′F}}G^{\text{liq}}_{\text{A′F}} + x_{\text{CsF}}G^{\text{liq}}_{\text{CsF}} + RT(x_{\text{A′F}}\ln x_{\text{A′F}} + x_{\text{CsF}}\ln x_{\text{CsF}}) + x_{\text{A′F}}x^{\upsilon}_{\text{CsF}}L^{\text{liq}}_{x_{\text{A′F}},x_{\text{CsF}}}(x_{\text{A′F}} - x_{\text{CsF}})^{\upsilon} \quad (\text{A′} = \text{K and Rb}) \tag{3}$$

where x_{AF}, x_{BeF_2}, $x_{\text{A′F}}$, and x_{CsF} are the mole fractions of AF, BeF_2, A′F, and CsF, respectively. $G^{\text{liq}}_{\text{AF}}$, $G^{\text{liq}}_{\text{BeF}_2}$, $G^{\text{liq}}_{\text{A′F}}$, and $G^{\text{liq}}_{\text{CsF}}$ are the Gibbs free energies of AF, BeF_2, A′F, and CsF, respectively. L^{liq} is the interaction parameter for the AF-BeF_2 and A′F-CsF systems, which is a function of temperature [57].

3.2.3 Intermediate phase

The intermediate phases, that is, $KBeF_3$, K_2BeF_4, K_3BeF_5, KBe_2F_5, $RbBeF_3$, Rb_2BeF_4, Rb_3BeF_5, $RbBe_2F_5$, $CsBeF_3$, Cs_2BeF_4, Cs_3BeF_5, and $CsBe_2F_5$, were thermodynamically described by the compound energy formalism, in which the Gibbs free energy is expressed as follows:

$$G^{\text{solid}}_{(\text{AF})_x(\text{BeF}_2)_y} = xG^{\text{o}}_{\text{AF}} + yG^{\text{o}}_{\text{BeF}_2} + \Delta_f H^{\text{o}}_{(\text{AF})_x(\text{BeF}_2)_y} - T\Delta_f S^{\text{o}}_{(\text{AF})_x(\text{BeF}_2)_y} \tag{4}$$

where G^{o}_{AF} and $G^{\text{o}}_{\text{BeF}_2}$ denote the Gibbs energies of the pure component AF and BeF_2, respectively. $\Delta_f H^{\text{o}}_{(\text{AF})_x(\text{BeF}_2)_y}$ and $\Delta_f S^{\text{o}}_{(\text{AF})_x(\text{BeF}_2)_y}$ represent the formation enthalpy and entropy, respectively, of the intermediate phase $(\text{AF})_x(\text{BeF}_2)_y$. $\Delta_f H^{\text{o}}_{(\text{AF})_x(\text{BeF}_2)_y}$ was predicted based on density functional theory (DFT) and was used as the initial value of thermodynamic optimization for the corresponding AF-BeF_2 (A = K, Rb, and Cs) systems shown in Table 2.

3.3 Theoretical prediction of formation enthalpy

The formation enthalpies of the intermediate compounds $ABeF_3$, A_2BeF_4, A_3BeF_5, and ABe_2F_5 (A = K, Rb, and Cs) were predicted based on the Open Quantum Materials Database (OQMD), which is a high-throughput database includess many DFT energies of compounds. The formation enthalpy was used as the initial value to optimize the sub-binary systems of the KF-RbF-CsF-BeF_2 system. The relevant calculated equations of the formation enthalpy are as follows based on the DFT single-point energy of the corresponding compounds:

$$\Delta_f H_{\text{ABeF}_3} = E_{\text{tot}}(\text{ABeF}_3) - E_{\text{tot}}(\text{AF}) - E_{\text{tot}}(\text{BeF}_2) \tag{5}$$

$$\Delta_f H_{\text{A}_2\text{BeF}_4} = E_{\text{tot}}(\text{A}_2\text{BeF}_4) - 2E_{\text{tot}}(\text{AF}) - E_{\text{tot}}(\text{BeF}_2) \tag{6}$$

$$\Delta_f H_{\text{A}_3\text{BeF}_5} = E_{\text{tot}}(\text{A}_3\text{BeF}_5) - 3E_{\text{tot}}(\text{AF}) - E_{\text{tot}}(\text{BeF}_2) \tag{7}$$

Table 2 The single point energies of the compounds from the KF-RbF-CsF-BeF_2 system

Compd	E_{tot} (eV/atom)	E_{tot} (kJ/mol)	Compd	E_{tot} (eV/atom)	E_{tot} (kJ/mol)
KF	–5.822	–560.775	$RbBeF_3$	–16.745	–1612.878
RbF	–5.710	–549.987	Rb_2BeF_4	–22.911	–2206.787
CsF	–5.662	–545.364	Rb_3BeF_5	–28.620	–2756.678
BeF_2	–10.545	–1015.694	$RbBe_2F_5$	–27.320	–2631.462
$KBeF_3$	–16.780	–1616.250	$CsBeF_3$	–16.825	–1620.584
K_2BeF_4	–23.016	–2216.901	Cs_2BeF_4	–22.932	–2208.810
K_3BeF_5	–28.836	–2777.483	Cs_3BeF_5	–28.593	–2754.078
KBe_2F_5	–27.328	–2632.233	$CsBe_2F_5$	–27.416	–2640.709

Table 3 Summary of the calculated thermodynamic parameters of the sub-binary systems of the KF-RbF-CsF-BeF_2 system

Systems	Phases	Models	Thermodynamic Parameters
KF-BeF_2	Liquid	$(KF, BeF_2)_{1.0}$	${}^0L^{Liquid}_{KF,BeF_2} = -84,718.8 + 10.910T$
			${}^1L^{Liquid}_{KF,BeF_2} = -37,828.8 + 25.000T$
			${}^2L^{Liquid}_{KF,BeF_2} = 21,813.6$
	K_3BeF_5	$(KF)_{3.0}(BeF_2)_{1.0}$	$G_{K_3BeF_5} = 3G_{KF} + G_{BeF_2} - 67,039.2$
	K_2BeF_4	$(KF)_{2.0}(BeF_2)_{1.0}$	$G_{K_2BeF_4} = 2G_{KF} + G_{BeF_2} - 40,000.0 - 23.063T$
	$KBeF_3$	$(KF)_{1.0}(BeF_2)_{1.0}$	$G_{KBeF_3} = G_{KF} + G_{BeF_2} - 34,842.2$
	KBe_2F_5	$(KF)_{1.0}(BeF_2)_{2.0}$	$G_{KBe_2F_3} = G_{KF} + 2G_{BeF_2} - 32,022.7 - 15.548T$
RbF-BeF_2	Liquid	$(RbF, BeF_2)_{1.0}$	${}^0L^{Liquid}_{RbF,BeF_2} = -106,785.0 + 6.637T$
			${}^1L^{Liquid}_{RbF,BeF_2} = -39,719.9 + 24.390T$
			${}^2L^{Liquid}_{RbF,BeF_2} = 29,064.2$
	Rb_3BeF_5	$(RbF)_{3.0}(BeF_2)_{1.0}$	$G_{Rb_3BeF_5} = 3G_{RbF} + G_{BeF_2} - 90,700.0$
	Rb_2BeF_4	$(RbF)_{2.0}(BeF_2)_{1.0}$	$G_{Rb_2BeF_4} = 2G_{RbF} + G_{BeF_2} - 61,540.0 - 23.017T$
	$RbBeF_3$	$(RbF)_{1.0}(BeF_2)_{1.0}$	$G_{RbBeF_3} = G_{RbF} + G_{BeF_2} - 47,850.0 - 3.561T$
	$RbBe_2F_5$	$(RbF)_{1.0}(BeF_2)_{2.0}$	$G_{RbBe_2F_3} = G_{RbF} + 2G_{BeF_2} - 53,400.0 - 14.334T$
CsF-BeF_2	Liquid	$(CsF, BeF_2)_{1.0}$	${}^0L^{Liquid}_{CsF,BeF_2} = -117,030.0 + 7.270T$
			${}^1L^{Liquid}_{CsF,BeF_2} = -36,015.8 + 20.374T$
			${}^2L^{Liquid}_{CsF,BeF_2} = 30,962.9$
	Cs_3BeF_5	$(CsF)_{3.0}(BeF_2)_{1.0}$	$G_{Cs_3BeF_5} = 3G_{CsF} + G_{BeF_2} - 98,868.7$
	Cs_2BeF_4	$(CsF)_{2.0}(BeF_2)_{1.0}$	$G_{Cs_2BeF_4} = 2G_{CsF} + G_{BeF_2} - 70,000.0 - 24.663T$
	$CsBeF_3$	$(CsF)_{1.0}(BeF_2)_{1.0}$	$G_{CsBeF_3} = G_{CsF} + G_{BeF_2} - 54,730.0 - 5.700T$
	$CsBe_2F_5$	$(CsF)_{1.0}(BeF_2)_{2.0}$	$G_{CsBe_2F_3} = G_{CsF} + 2G_{BeF_2} - 64,208.0 - 13.000T$
KF-CsF	Liquid	$(KF, CsF)_{1.0}$	${}^0L^{Liquid}_{KF,CsF} = 7,220.0 - 2.014T$
			${}^1L^{Liquid}_{KF,CsF} = -27,050.0 + 24.858T$
	Halite	$(KF, CsF)_{1.0}$	${}^0L^{Halite}_{KF,CsF} = 22,641.0 + 7.531T$
			${}^1L^{Halite}_{KF,CsF} = 6,223.0 - 0.415T$
RbF-CsF	Liquid	$(RbF, CsF)_{1.0}$	${}^0L^{Liquid}_{RbF,CsF} = -20,438.8 + 15.102T$

L: Interaction parameter between the binary systems, expressed as $L = a + b \times T$ (*T*: temperature)

G: Gibbs free energy

$$\Delta_f H_{ABe_2F_5} = E_{tot}(ABe_2F_5) - E_{tot}(AF) - 2E_{tot}(BeF_2) \quad (8)$$

where $E_{tot}(AF)$, $E_{tot}(BeF_2)$, $E_{tot}(ABeF_3)$, $E_{tot}(A_2BeF_4)$, $E_{tot}(A_3BeF_5)$, and $E_{tot}(ABe_2F_5)$ are the single points of AF, BeF_2, $ABeF_3$, A_2BeF_4, A_3BeF_5 and ABe_2F_5 (A = K, Rb, and Cs), respectively, as listed in Table 2.

3.4 AIMD

AIMD simulations were used to investigate the structure and properties of KF-RbF-CsF-BeF_2 systems with two different proportions (i.e., 3.50–28.92–21.78–45.80 mol% and 1.80–35.42–52.40–10.38 mol%), which are denoted as Mixtures 1 and 2, respectively, in the following sections. The initial simulation systems for the molten salts were constructed using a random insertion method, based on the densities predicted in the previous section. Mixtures 1 and 2 consisted of 140 atoms (2 K, 17 Rb, 12 Cs, 26 Be, and 83 F) and 118 atoms (1 K, 20 Rb, 29 Cs, 6 Be, and 62 F) atoms, respectively. Because the temperature has little effect on the structure of molten salts [58], only the 650 °C was investigated in this study.

AIMD based on DFT was performed using the Vienna Ab initio Simulation Package [59–62]. The exchange–correlation energy was described using the Perdew-Burke-Ernzerhof functional of the generalized gradient approximation [63, 64]. The electron–ion core interactions were described by the projector-augmented plane-wave [65] method, and an energy cutoff of 600 eV for the plane-wave expansion of the wave functions was used. The Γ point was chosen to sample the Brillouin zone [66]. A time step of 1.0 fs and a simulation temperature of 650 °C were used for all AIMD simulations, and the convergence criterion for the total energy was set at 10^{-5} eV.

The simulation process was as follows. First, 5 ps simulations for the two systems were conducted in an NPT ensemble with a Langevin thermostat to optimize the cell volumes using the method of Parrinello and Rahman [67, 68]. The

corresponding equilibrium volumes were then obtained from the average of the last 3000 steps. Finally, 15 ps simulations for the two systems based on the equilibrium volumes were performed in an NVT ensemble with a Nosé thermostat [69, 70]. The systems reached equilibrium within 2 ps, and the structures and properties of the molten salt systems were obtained by analyzing the last 10,000 steps of the simulation.

The partial RDF is important for describing the atomic configuration in liquid systems and is defined as the probability of finding another atom at a distance r from a center reference atom, as shown in Eq. (9) [71]:

$$g_{i,j}(r) = \frac{\mathrm{d}n_j(r)}{4\pi r^2 \rho_j \mathrm{d}r} \tag{9}$$

where Δn_j is the number of j atoms in the spherical shell between radii $r - 0.5\Delta r$ and $r + 0.5\Delta r$, i stands for the center atoms, and ρ_j is the atomic number density of element j in the system. In a molten salt system, the first shell CNs of the central atom can be obtained by integrating the RDF within the cutoff radius (R_{cut}), as expressed in Eq. (10) [71]:

$$CN_{i,j} = \int_0^{R_{\mathrm{cut}}} 4\pi r^2 \rho_j g_{i,j}(r) \mathrm{d}r \tag{10}$$

where R_{cut} is the radius corresponding to the first valley of the RDF. The ADF describes the three-body correlation information and is defined as the average of the angles between the central atom and any two adjacent coordinated atoms in the system, as shown in Eq. (11) [72]:

$$\theta_{jik} = \left\langle \cos^{-1} \frac{r_{ij}^2 + r_{ik}^2 - r_{jk}^2}{2 r_{ij} r_{ik}} \right\rangle \tag{11}$$

Table 4 Formation enthalpies of the intermediate compounds from the sub-binary systems of KF-RbF-CsF-BeF_2 system in the present work and calculated values from the OQMD

Binary system	Compounds	OQMD (kJ/mol)	This work (kJ/mol)
KF-BeF_2	K_3BeF_5	–39.780	–67.039
	K_2BeF_4	–79.656	–40.000
	$KBeF_3$	–79.464	–34.842
	KBe_2F_5	–40.069	–32.022
RbF-BeF_2	Rb_3BeF_5	–47.197	–90.700
	Rb_2BeF_4	–91.119	–61.540
	$RbBeF_3$	–91.022	–47.850
	$RbBe_2F_5$	–50.086	–53.400
CsF-BeF_2	Cs_3BeF_5	–59.526	–98.868
	Cs_2BeF_4	–102.388	–70.000
	$CsBeF_3$	–102.292	–54.730
	$CsBe_2F_5$	–63.956	–64.208

where j and k are the adjacent coordinated atoms within R_{cut} of central atom i. The self-diffusion coefficients can be used to depict the transport characteristics of the molten salt and reflect the diffusivity of each component in the molten salt. They can be calculated using the mean square displacement (MSD) and Einstein formula, according to Eqs. (12) and (13) [72]:

$$MSD_A(t) = \frac{1}{N_A} \sum_{i=1}^{N_A} |r_i(t) - r_i(0)|^2 \tag{12}$$

$$D_A = \lim_{t \to \infty} \frac{1}{6t} MSD_A(t) \tag{13}$$

where $r_i(t)$ is the displacement of an A-type atom at time t and N_A represents the total number of elements A.

4 Results and discussion

4.1 Binary system

All phase diagrams were plotted using the PanPhaseDiagram module of the PANDAT software based on the optimized thermodynamic parameters listed in Table 3. The calculated phase diagrams will be discussed in the following section. The optimized formation enthalpies of the intermediate compounds from the sub-binary systems of the KF-RbF-CsF-BeF_2 system and the calculated values from the OQMD are shown in Table 4. The calculated formation enthalpy agrees with most values from the OQMD, although some deviation between them exists owing to the different temperatures used (i.e., the values in the OQMD were obtained at 0 K, and the present optimized data were acquired at 298.15 K). Table 5 compares the calculated values of the key invariant points with the experimental data of the sub-binary systems of the KF-RbF-CsF-BeF_2 system.

Figures 1, 2, 3,4 and 5 show the calculated phase diagrams of the AF-BeF_2 (A = K, Rb, and Cs) and A′F-CsF (A′ = K and Rb) systems with the corresponding experimental data [21, 47, 53, 54]. As clearly observed from Fig. 1, the calculated value of the KF-BeF_2 system shows a high level of consistency with the experimental data from Moore et al., especially for the invariable point. For instance, the congruent melting temperatures of K_3BeF_5, K_2BeF_4, and KBe_2F_5 at 736.7 K, 784.7 K, and 357.1 K, respectively, are in excellent agreement with the experimental values of 740.0 K, 787.0 K, and 358.0 K, respectively [21]. As shown in Fig. 2, good agreement exists between the calculated values of the RbF-BeF_2 system and the experimental data from Moore et al., except for some small deviation in the liquidus of the BeF_2 end

Table 5 Comparison between the calculated values of key points and experimental data of the sub-binary systems of the KF-RbF-CsF-BeF_2 system

System	Reaction	Invariant point		Reference
KF-BeF_2		T (°C)	χ_{BeF_2}	
	Liquid → K_3BeF_5 + KF	716.8	0.186	[*]
		720.0	0.190	Moore et al
	Liquid → K_3BeF_5	736.7	0.250	[*]
		740.0	0.250	Moore et al
	Liquid → K_2BeF_4 + K_3BeF_5	736.1	0.260	[*]
		730.0	0.270	Moore et al
	Liquid → K_2BeF_4	784.7	0.333	[*]
		787.0	0.333	Moore et al
	Liquid + K_2BeF_4 → $KBeF_3$	391.3	0.525	[*]
		390.0	0.520	Moore et al
	Liquid → $KBeF_3$ + KBe_2F_5	323.6	0.606	[*]
		330.0	0.590	Moore et al
	Liquid → KBe_2F_5	357.1	0.667	[*]
		358.0	0.667	Moore et al
	Liquid → BeF_2 + KBe_2F_5	319.6	0.744	[*]
		323.0	0.725	Moore et al
RbF-BeF_2	Reaction	T (°C)	χ_{BeF_2}	Reference
	Liquid → RbF + Rb_3BeF_5	671.0	0.155	[*]
		675.0	0.160	Moore et al
	Liquid → K_3BeF_5	725.0	0.250	[*]
		725.0	0.250	Moore et al
	Liquid → Rb_2BeF_4 + Rb_3BeF_5	724.8	0.254	[*]
		720.0	0.270	Moore et al
	Liquid → Rb_2BeF_4	800.2	0.333	[*]
		800.0	0.333	Moore et al
	Liquid + Rb_2BeF_4 → $RbBeF_3$	442.2	0.505	[*]
		442.0	0.505	Moore et al
	Liquid → $RbBeF_3$ + $RbBe_2F_5$	393.4	0.580	[*]
		383.0	0.610	Moore et al
	Liquid → $RbBe_2F_5$	464.4	0.667	[*]
		464.0	0.667	Moore et al
	Liquid → BeF_2 + $RbBe_2F_5$	387.3	0.787	[*]
		397.0	0.810	Moore et al
CsF-BeF_2	Reaction	T (°C)	χ_{BeF_2}	Reference
	Liquid → CsF + Cs_3BeF_5	590.0	0.144	[*]
		598.0	0.140	Breusov et al
	Liquid + Cs_2BeF_4 → Cs_3BeF_5	662.2	0.232	[*]
		659.0	0.235	Breusov et al
	Liquid → Cs_2BeF_4	793.0	0.333	[*]
		793.0	0.333	Breusov et al
	L → $CsBeF_3$ + Cs_2BeF_4	459.8	0.479	[*]
		449.0	0.480	Breusov et al
	Liquid → $CsBeF_3$	465.0	0.500	[*]
		475.0	0.500	Breusov et al
	Liquid → $CsBeF_3$ + $CsBe_2F_5$	388.7	0.582	[*]
		393.0	0.584	Breusov et al
	Liquid → $CsBe_2F_5$	480.0	0.667	[*]
		480.0	0.667	Breusov et al
	Liquid → BeF_2 + $CsBe_2F_5$	362.5	0.792	[*]

Table 5 (continued)

System	Reaction	Invariant point		Reference
KF-BeF_2		T (°C)	χ_{BeF_2}	
		367.0	0.775	Breusov et al
KF-CsF	Reaction	T (°C)	χ_{CsF}	Reference
	Liquid → KF + (K,Cs)F	624.3	0.571	[*]
		625.0	0.570	Samuseva et al
	Halite → (K,Cs)F#1 + (K,Cs)F#2	624.3	0.950	[*]
		625.0	0.850	Samuseva et al
RbF-CsF	Reaction	T (°C)	χ_{CsF}	Reference
	Liquid → RbF + CsF	670.8	0.684	[*]
		673.85	0.726	Beneš et al
		677.85	0.750	Beneš et al

*: This work

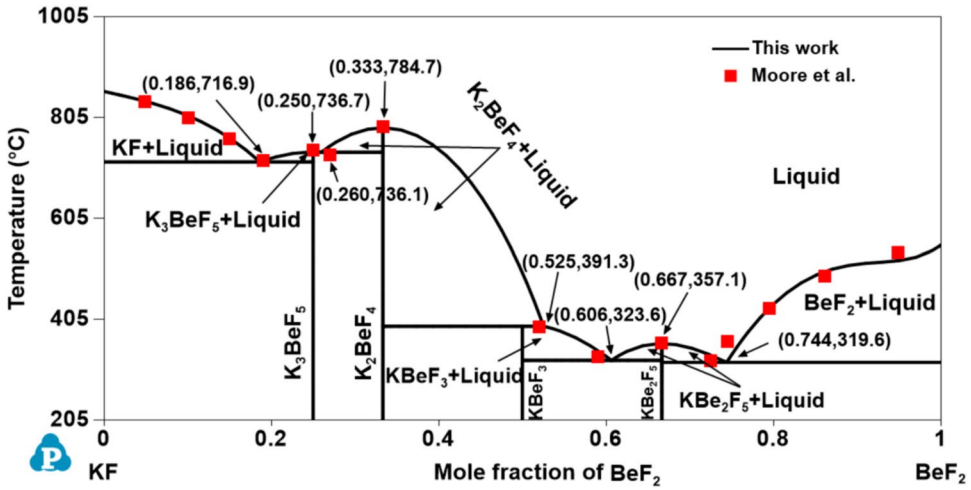

Fig. 1 Calculated phase diagram of the KF-BeF_2 system with experimental data from Moore et al. (Color figure online)

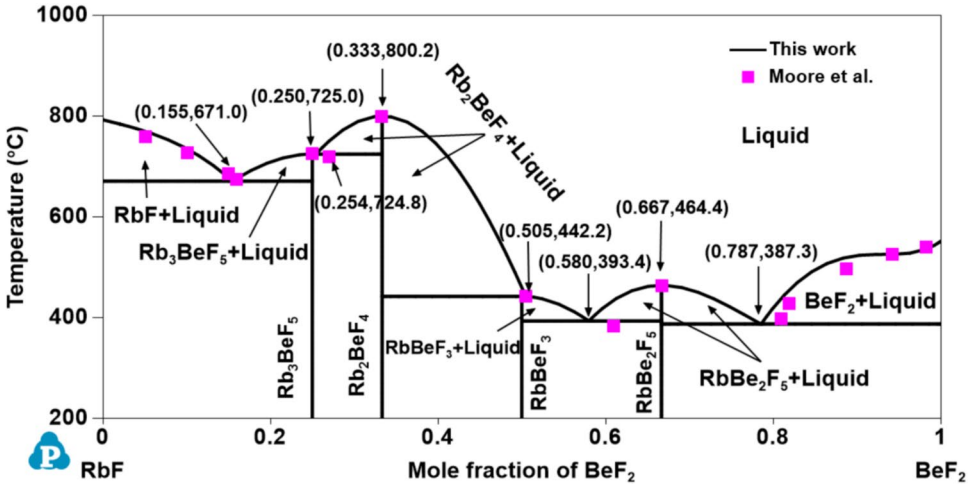

Fig. 2 Calculated phase diagram of the RbF-BeF_2 system with experimental data from Moore et al. (Color figure online)

member. Similarly, the calculated melting temperatures of the intermediate phases Rb_3BeF_5, Rb_2BeF_4, and Rb_2BeF_4 at 725.0 K, 800.0 K, and 464.0 K, respectively, are nearly equal to the experimental values of 725.0 K, 800.2 K, and 464.4 K, respectively [21]. As shown in Fig. 3, the calculated phase diagram of the CsF-BeF_2 system is in

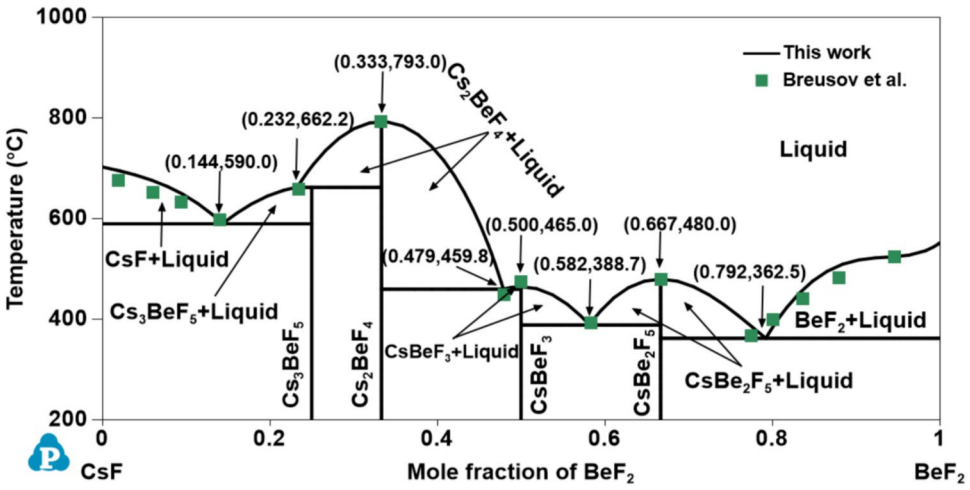

Fig. 3 Calculated phase diagram of the CsF-BeF_2 system with experimental data from Breusov et al. (Color figure online)

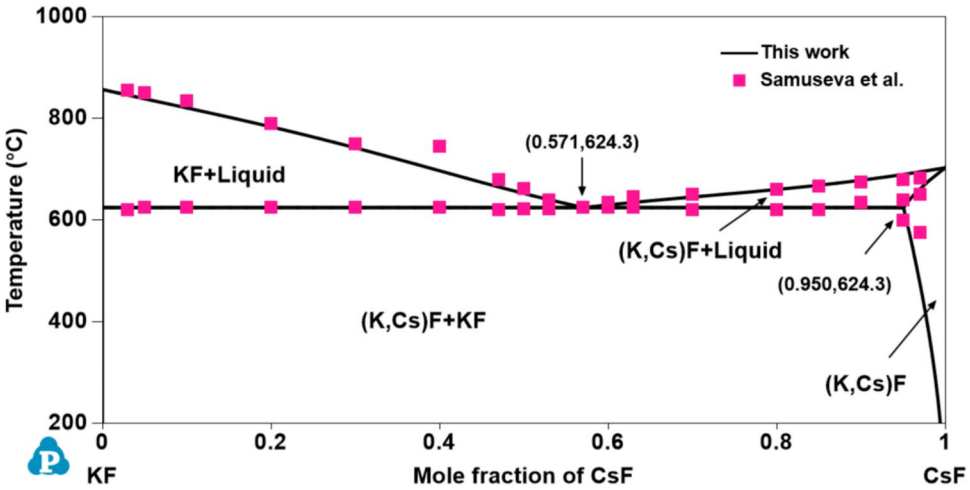

Fig. 4 Calculated phase diagram of the KF-CsF system with experimental data from Samuseva et al. (Color figure online)

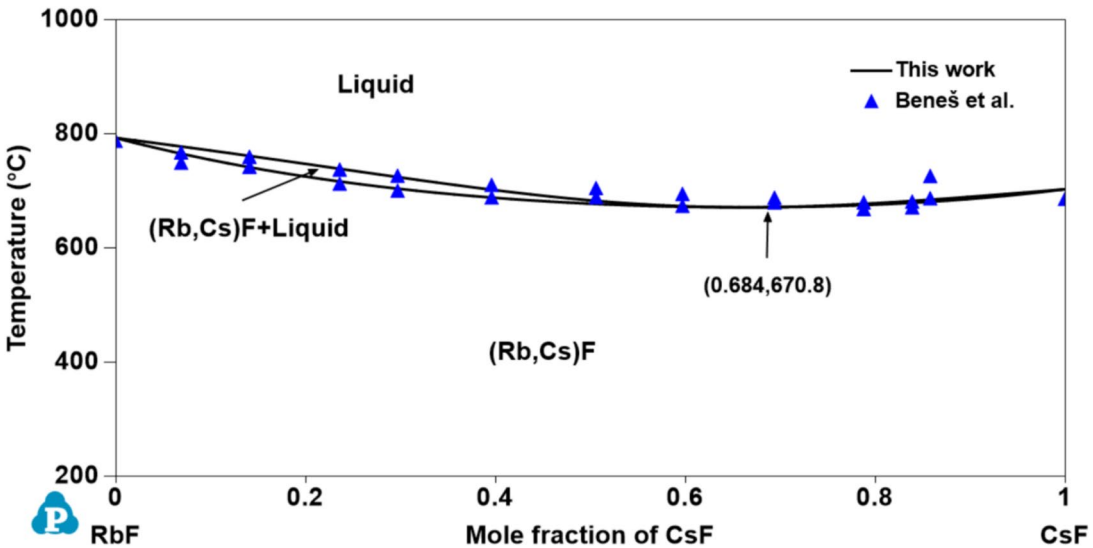

Fig. 5 Calculated phase diagram of the RbF-CsF system with experimental data from Beneš et al. (Color figure online)

good agreement with the experimental data from Breusov et al. [47], although some slight deviation is present on the rich-BeF_2 side. In particular, the calculated values of the key invariant points (i.e., 598.0 °C and 0.140 mol BeF_2, 793.0 °C and 0.333 mol BeF_2, and 480.0 °C and 0.667 mol BeF_2) are almost the same as the experimental data (590.0 °C and 0.144 mol BeF_2, 793.0 °C and 0.333 mol BeF_2, and 480.0 °C and 0.667 mol BeF_2), as shown in Table 5. As notably demonstrated by Fig. 4, the present calculated phase diagram of the KF-CsF system is in satisfactory agreement with the experimental data from Samuseva et al. [53], where the present calculated eutectic point of 624.3 °C and 0.571 mol CsF is almost the same as the experimental point of 625.0 °C and 0.570 mol CsF. The optimized solid solution point of 624.3 °C and 0.950 mol CsF also agrees well with the experimental point of 625.0 °C and 0.850 mol CsF. Figure 5 displays the optimized phase diagram of the RbF-CsF system, where the optimized value corresponds well with the experimental data from Beneš et al. [54]. The present optimized minimum temperature on the liquidus (670.8 °C) agrees with the experimental results from Beneš et al. (677.85 °C and 673.85 °C).

4.2 Ternary system

The liquidus projections of the ternary BeF_2-KF-RbF, BeF_2-CsF-KF, BeF_2-CsF-RbF, and CsF-KF-RbF systems were calculated based on the thermodynamic parameters of the binary system using an extrapolation model. Figure 6(a–d) show the liquidus projections of these ternary systems with the primary phases and temperatures formed during the solidification process. In Fig. 6(d), no ternary invariant point is observed for the CsF-KF-RbF system

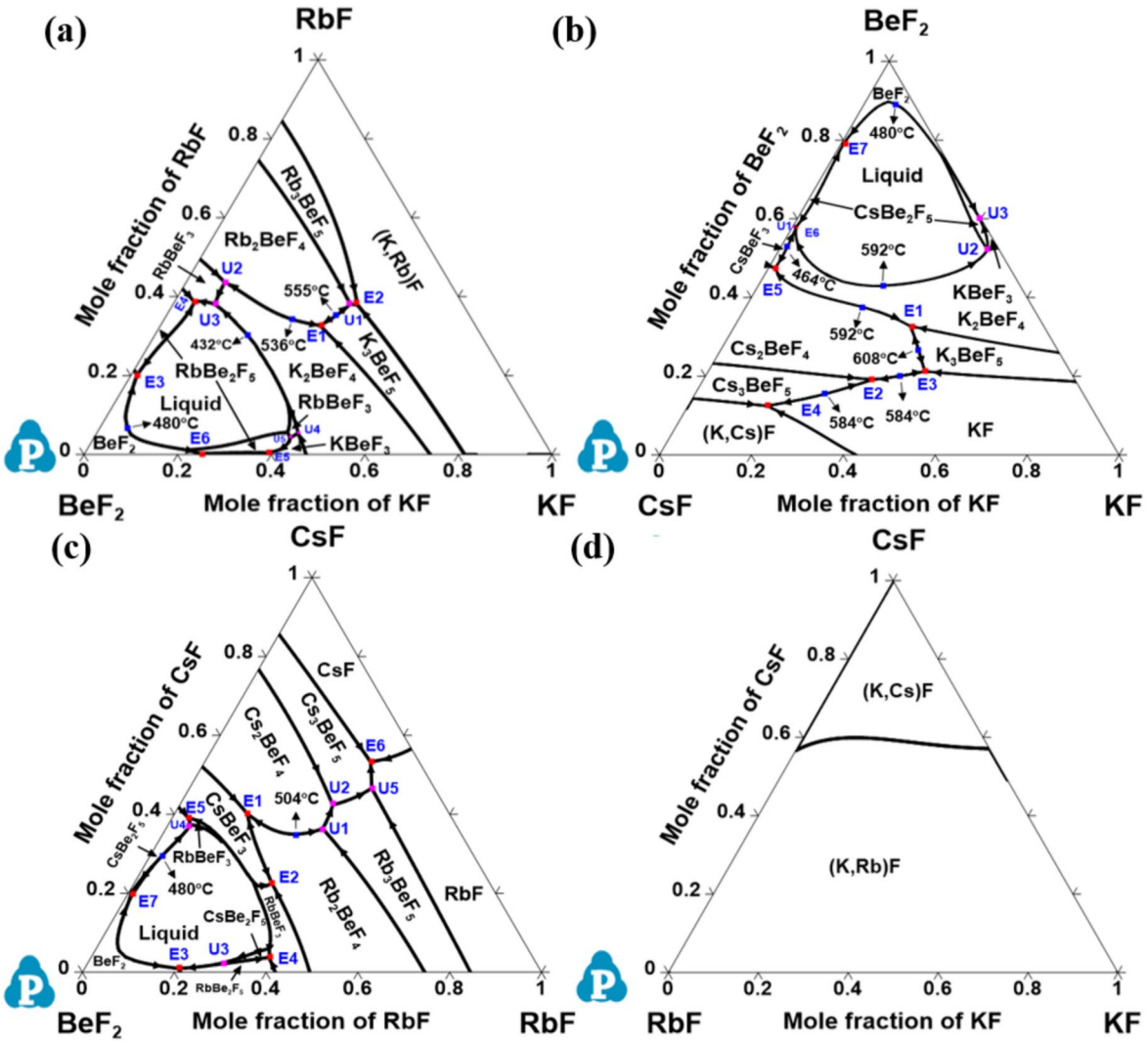

Fig. 6 (Color online) Calculated liquidus projections of the ternary (**a**) BeF_2-KF-RbF, (**b**) BeF_2-CsF-KF, (**c**) BeF_2-CsF-RbF, and (**d**) CsF-KF-RbF systems

Table 6 Calculated invariant reactions and temperatures of the BeF_2-KF-RbF, BeF_2-CsF-KF, BeF_2-CsF-RbF, and CsF-KF-RbF systems

Ternary system (A-B-C)	Reaction type	Temp. (°C)	χ_A	χ_B	χ_C
BeF_2-KF-RbF	$Liquid \xrightarrow{E1} K_2BeF_4 + Rb_2BeF_4 + K_3BeF_5$	537.7	0.3322	0.3405	0.3273
	$Liquid + Rb_2BeF_4 \xrightarrow{U1} Rb_3BeF_5 + K_3BeF_5$	529.1	0.2402	0.3786	0.3812
	$Liquid \xrightarrow{E^2} (K, Rb)F + Rb_3BeF_5 + K_3BeF_5$	526.8	0.2258	0.3950	0.3792
	$Liquid + Rb_2BeF_4 \xrightarrow{U2} RbBeF_3 + K_2BeF_4$	423.3	0.4809	0.0823	0.4368
	$Liquid + K_2BeF_4 \xrightarrow{U3} RbBeF_3 + Liquid$	404.4	0.5298	0.0896	0.3806
	$Liquid \xrightarrow{E3} RbBe_2F_5 + BeF_2 + Liquid$	382.3	0.7861	0.0128	0.2011
	$Liquid \xrightarrow{E4} RbBe_2F_5 + RbBeF_3 + Liquid$	382.1	0.5703	0.0427	0.3870
	$Liquid + K_2BeF_4 \xrightarrow{U4} RbBeF_3 + KBeF_3$	378.0	0.5154	0.4309	0.0537
	$Liquid + RbBeF_3 \xrightarrow{U5} RbBe_2F_5 + KBeF_3$	371.4	0.5376	0.4193	0.0431
	$Liquid \xrightarrow{E5} RbBe_2F_5 + KBeF_3 + KBe_2F_5$	321.7	0.6064	0.3892	0.0044
	$Liquid \xrightarrow{E5} RbBe_2F_5 + BeF_2 + KBe_2F_5$	318.0	0.7442	0.2528	0.0030
BeF_2-CsF-KF	$Liquid \xrightarrow{EI} K_2BeF_4 + Cs_2BeF_4 + K_3BeF_5$	597.7	0.3276	0.2907	0.3817
	$Liquid \xrightarrow{E2} KF + Cs_2BeF_4 + Cs_3BeF_5$	578.9	0.1917	0.4399	0.3684
	$Liquid \xrightarrow{E3} KF + Cs_2BeF_4 + K_3BeF_5$	573.4	0.2126	0.3164	0.4710
	$Liquid \xrightarrow{E4} KF + Cs_3BeF_5 + (K, Cs)F$	553.3	0.1248	0.7035	0.1717
	$Liquid \xrightarrow{E5} K_2BeF_4 + CsBeF_5 + Cs_2BeF_4$	453.5	0.4746	0.5108	0.0146
	$Liquid + K_2BeF_4 \xrightarrow{U1} CsBeF_3 + Liquid$	392.6	0.5189	0.0282	0.4529
	$Liquid \xrightarrow{E6} CsBeF_3 + CsBe_2F_5 + Liquid$	385.0	0.5240	0.0253	0.4507
	$Liquid + K_2BeF_4 \xrightarrow{U2} CsBeF_3 + KBeF_3$	383.9	0.5214	0.0250	0.4536
	$Liquid + CsBeF_3 \xrightarrow{U3} KBeF_3 + CsBe_2F_5$	383.2	0.5239	0.0247	0.4514
	$Liquid \xrightarrow{E7} CsBe_2F_5 + BeF_2 + Liquid$	359.8	0.7631	0.0056	0.2313
BeF_2-CsF-RbF	$Liquid + Rb_2BeF_4 \xrightarrow{U1} Cs_2BeF_4 + Rb_3BeF_5$	495.0	0.2946	0.3639	0.3415
	$Liquid + Cs_2BeF_4 \xrightarrow{U2} Cs_3BeF_5 + Rb_3BeF_5$	469.8	0.2428	0.4240	0.3332
	$Liquid + CsBe_2F_5 \xrightarrow{U3} RbBe_2F_5 + Liquid$	446.2	0.7025	0.0191	0.2784
	$Liquid \xrightarrow{E1} Rb_2BeF_4 + CsBeF_3 + Cs_2BeF_4$	409.1	0.4399	0.4016	0.1585
	$Liquid \xrightarrow{E2} Rb_2BeF_4 + RbBeF_3 + CsBeF_3$	400.6	0.4746	0.2257	0.2997
	$Liquid1 + Liquid2 \xrightarrow{U4} CsBe_2F_5 + RbBeF_5$	387.8	0.5635	0.0597	0.3768
	$Liquid + Rb_3BeF_5 \xrightarrow{U5} Cs_3BeF_5 + RbF$	386.2	0.1366	0.4665	0.3969
	$Liquid \xrightarrow{E3} RbBe_2F_5 + BeF_2 + Liquid$	383.4	0.7871	0.0098	0.2031
	$Liquid \xrightarrow{E4} CsBe_2F_5 + RbBeF_3 + RbBe_2F_5$	382.8	0.5745	0.0377	0.3878
	$Liquid \xrightarrow{E5} CsBe_2F_5 + RbBeF_3 + CsBeF_3$	374.9	0.5734	0.3894	0.0372
	$Liquid \xrightarrow{E6} Cs_3BeF_5 + RbF + CsF$	369.5	0.1057	0.5336	0.3607
	$Liquid \xrightarrow{E7} RbBe_2F_5 + CsBe_2F_5 + BeF_2$	359.4	0.7922	0.2018	0.0060
CsF-KF-RbF	$Liquid + (K, Rb)F \xrightarrow{U1} KF + (K, Cs)F$	624.3	0.5716	0.4284	–
	$(K, Rb)F + CsF \xrightarrow{U2} Liquid + (K, Cs)F$	450.0	0.5664	–	0.4336

because of the inherent properties of its sub-binary system, that is, KF-RbF and RbF-CsF are isomorphous systems with a minimum in the liquids. The BeF_2-KF-RbF system shown in Fig. 6(a) is characterized by six eutectic and five transition reactions, and the BeF_2-CsF-KF system features seven eutectic reactions and three transition reactions, as shown in Fig. 6(b). The BeF_2-CsF-RbF system is also characterized by seven eutectic reactions, but has five transition reactions, as depicted in Fig. 6(c). The results show that complex reactions can occur in the BeF_2-KF-RbF, BeF_2-CsF-KF, and BeF_2-CsF-RbF systems during the solidification process. The detailed invariant reactions and temperatures of the BeF_2-KF-RbF, BeF_2-CsF-KF, BeF_2-CsF-RbF, and CsF-KF-RbF systems are listed in Table 6.

4.3 Quaternary system

The quaternary KF-RbF-CsF-BeF_2 system was further investigated in terms of the thermodynamic databases of its sub-binary systems using an extrapolation model. The component proportions of the quaternary KF-RbF-CsF-BeF_2 system were predicted based on its melting temperature. Table 7 shows the detailed melting point data with the corresponding component proportions; the melting temperature is not higher than 450.0 °C, which is a commonly acceptable temperature for the coolant in an MSR. As shown in Table 7, 10 kinds of KF-RbF-CsF-BeF_2 systems with different proportions were obtained through the thermodynamic calculations, where the content of BeF_2 varies from approximately 10 to 60 mol%. BeF_2-based molten salts commonly have much higher viscosities when the BeF_2 content of the molten salt is high (especially when the BeF_2 content is greater than 50 mol%). Therefore, the proportion of BeF_2 should be maintained within an acceptable range for practical applications. Thus, the quaternary KF-RbF-CsF-BeF_2 systems labeled No. (1)–(9) were chosen as relatively appropriate heat transfer media for MSRs based on the melting temperature ($T_{m.p.} \leq 450$ °C) and viscosity (i.e., BeF_2 content ≤ 50 mol%). The local structures of the KF-RbF-CsF-BeF_2 molten salts with different portions will be

Table 7 Predicted melting temperature (i.e., $T_{m.p.} \leq 450$ °C) with corresponding component proportions of the quaternary KF-RbF-CsF-BeF_2 system

Ternary system (A-B-C)	No.	Temp. (°C)	χ_A	χ_B	χ_C	χ_D
KF-RbF-CsF-BeF_2	(1)	450.0	0.0180	0.3542	0.5240	0.1038
	(2)	450.0	0.3814	0.0043	0.0200	0.5943
	(3)	450.0	0.0200	0.0365	0.3816	0.5619
	(4)	378.7	0.0102	0.0368	0.3854	0.5676
	(5)	394.0	0.0806	0.3565	0.0347	0.5282
	(6)	450.0	0.1665	0.3232	0.0314	0.4789
	(7)	450.0	0.0327	0.1533	0.3885	0.4255
	(8)	431.5	0.0257	0.1544	0.3913	0.4286
	(9)	402.6	0.0350	0.2892	0.2178	0.4580
	(10)	450.0	0.0658	0.2800	0.2108	0.4434

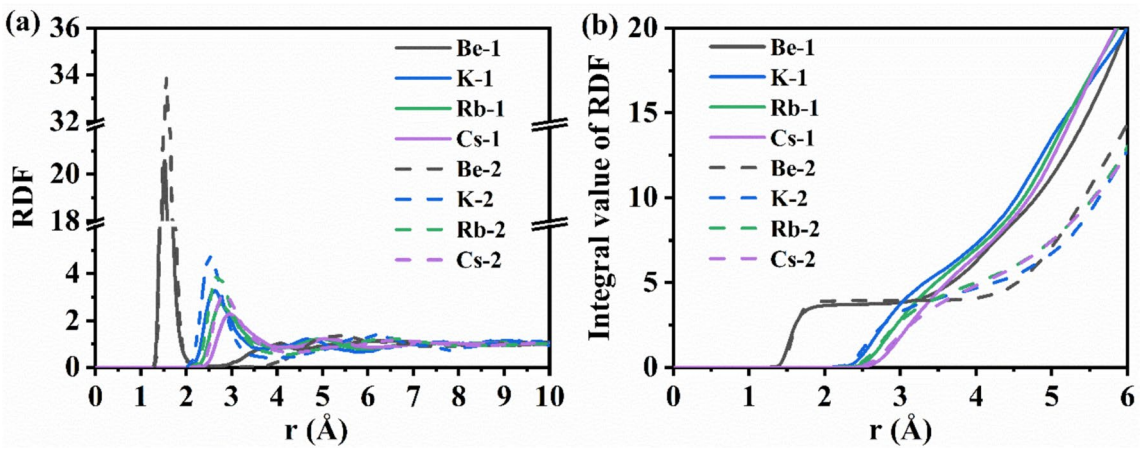

Fig. 7 (**a**) RDFs of Be-F, K-F, Rb-F, and Cs-F pairs, and (**b**) their corresponding integral curves. The solid and dashed lines represent the cases of Mixtures 1 and 2, respectively. (Color Figure online)

further discussed based on first-principles calculations in the following section.

4.3.1 RDFs

In the AIMD calculations, the NPT ensemble simulations revealed that the equilibrium densities of Mixture 1 (KF-RbF-CsF-BeF_2, 3.50–28.92–21.78–45.80 mol%) and Mixture 2 (KF-RbF-CsF-BeF_2, 1.80–35.42–52.40–10.38 mol%) at 650 °C were 2.22 g/cm^3 and 2.72 g/cm^3, respectively. Figure 7(a) presents the RDFs of the Be-F, K-F, Rb-F, and Cs-F ion pairs in the two molten salt systems. These systems exhibit some similar features. The RDFs for all cation–anion pairs have sharper and stronger first peaks, indicating an ordered arrangement of F^- around Be^{2+}, K^+, Rb^+, and Cs^+. As the distance increases, the fluctuations of the RDFs gradually decrease and tend towards 1, reflecting the short-range order and long-range disorder in the microstructure of the molten salt systems. The highest first peak is observed for the Be-F ion pair, with the peak valley being almost zero, indicating a strong interaction between Be^{2+} and F^-. This finding suggests that F^- has more difficulty escaping from the coordination shell of Be^{2+} compared to those of other cations. The relative interaction strength of the cations with F^- in the same system can be inferred from the heights of the first peaks for each ion pair as follows: $Be^{2+} > K^+ > Rb^+ > Cs^+$. This correlates with the average charge of the cations, and a higher charge results in stronger interactions with F^-. Be^{2+} has the highest valence state and the smallest ionic radius among the cations, resulting in the strongest interaction. K^+, Rb^+, and Cs^+ have the same valence state, and their interaction strength with F^- decreases with increasing ionic radius: $Cs^+ > Rb^+ > K^+$.

The first peak of the RDF of each ion pair in Mixture 1 is lower than that in Mixture 2, indicating a more ordered arrangement of F^- around the cations in Mixture 2. The first peak position of the RDF typically represents the average bond length of the ion pair (Table 8). The peak positions of Be-F, K-F, Rb-F, and Cs-F in Mixture 1 are 1.55, 2.63, 2.77, and 2.95, respectively, and 1.57, 2.51, 2.69, and 2.83 in Mixture 2. With decreasing Be^{2+} content in Mixture 2, the average bond length of the Be-F ion pairs remains relatively unchanged, which is attributed to the strong interaction between Be^{2+} and F^-. The Be–F bond length is almost the same as that in the LiF-BeF_2 system [48]. The peak positions for the other cation–anion pairs decrease significantly in Mixture 2 compared to those in Mixture 1. The bond length also reflects the strength of the ion pairs; shorter bond lengths indicate stronger interactions between the same ion pairs. Thus, the interactions between the cations and F^- in Mixture 2 are stronger than those in Mixture 1. Because the concentration of Be^{2+} is higher in Mixture 1, F^- preferentially binds with Be^{2+}, thereby weakening its interactions with the other cations.

Table 8 First peak position and cutoff radius (R_{cut}) of the RDF (Å) and CNs of cations

	Mixture 1			Mixture 2		
	First peak	R_{cut}	CNs	First peak	R_{cut}	CNs
Be-F	1.55	2.45	3.72	1.57	2.43	3.93
K-F	2.63	3.69	6.14	2.51	3.61	4.23
Rb-F	2.77	3.97	6.73	2.69	3.93	4.89
Cs-F	2.95	4.11	7.03	2.83	4.09	5.01

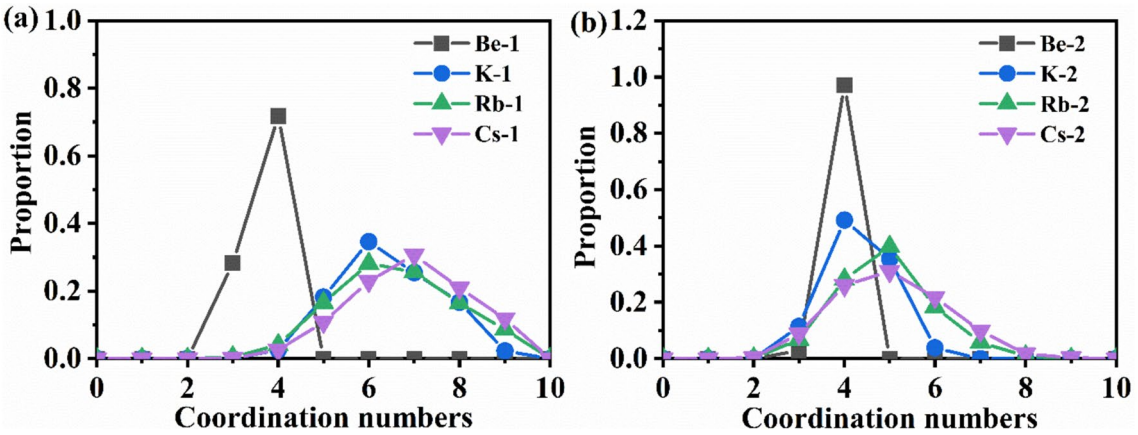

Fig. 8 Proportions of CNs in **a** Mixture 1 and **b** Mixture 2. (Color figure online)

4.3.2 CNs

The CNs were obtained by integrating the RDFs of the ion pairs. Figure 7(b) shows the integral values of the RDF for the Be-F, K-F, Rb-F, and Cs-F pairs in the two molten salt systems. In general, the values corresponding to R_{cut} in Fig. 7(b) are the CNs, and the calculated CNs for each cation are listed in Table 6. In Mixture 1, the CNs of Be^{2+}, K^+, Rb^+, and Cs^+ are 3.72, 6.14, 6.73, and 7.03, respectively, and in Mixture 2, they are 3.93, 4.23, 4.89, and 5.01, respectively. Except for Be^{2+}, the CNs of the other cations in Mixture 1 are larger than those in Mixture 2, which is mainly owing to the higher concentration of F^- in Mixture 1. Additionally, for the K-F, Rb-F, and Cs-F ion pairs, the integral curves do not exhibit a clear plateau near R_{cut}, as is present for the Be-F pair. Therefore, these cations can localize F^- within a certain range, but there are no compact complex structures as Be^{2+}. Furthermore, the proportions of CNs for all cations within the R_{cut} were calculated to study the coordination preference with F^-, as shown in Fig. 8. Be^{2+} predominantly forms fourfold coordination structures in both systems, like in the LiF-BeF_2 system, where Be^{2+} is dominated by $[BeF_4]^{2-}$ [48]. For the K-F, Rb-F, and Cs-F ion pairs, the coordinated structures in their first coordination shells range from twofold to ninefold. The sixfold and sevenfold coordination structures account for the largest two portions in Mixture 1, whereas the fourfold and fivefold structures account for the largest portions in Mixture 2.

4.3.3 ADFs

To describe the three-body correlations of the ions in the molten salt systems further, the ADFs of F-Be-F, F-K-F, F-Rb-F, and F-Cs-F were calculated, as shown in Fig. 9. The angle of F-Be-F is mainly distributed in the range of 90°–130° both in Mixtures 1 and 2, with the maximum peak at approximately 109°. This corresponds to the slightly distorted tetrahedral $[BeF_4]^{2-}$, consistent with that in the LiF-BeF_2 system [1]. For the F-K-F, F-Rb-F, and F-Cs-F pairs, the angle distribution range is wide and different from that for the F-Be-F pair in both Mixtures 1 and 2, and various coordination structures ranging from twofold to ninefold exist, as shown in Fig. 9. This is because K^+, Rb^+, and Cs^+ do not form compact ion structures with F^-.

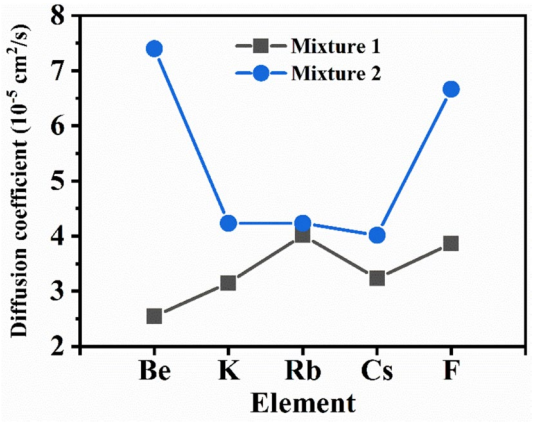

Fig. 10 Diffusion coefficients of the ions in two molten salt systems at 650 °C. (Color figure online)

4.3.4 Diffusion coefficient

The diffusion coefficients of the ions were calculated using Eqs. (12) and (13), as illustrated in Fig. 10. The diffusion coefficients of Be^{2+}, K^+, Rb^+, Cs^+, and F^- in Mixture 2 are 7.4×10^{-5}, 4.23×10^{-5}, 4.23×10^{-5}, 4.01×10^{-5}, and 6.67×10^{-5} cm^2/s, respectively. Owing to their small ionic radii and masses, Be^{2+} and F^- exhibit higher mobilities than the other ions. Conversely, characterized by its larger ionic radius and mass, Cs^+ exhibits the lowest diffusion coefficient. As the proportion of BeF_2 increases in

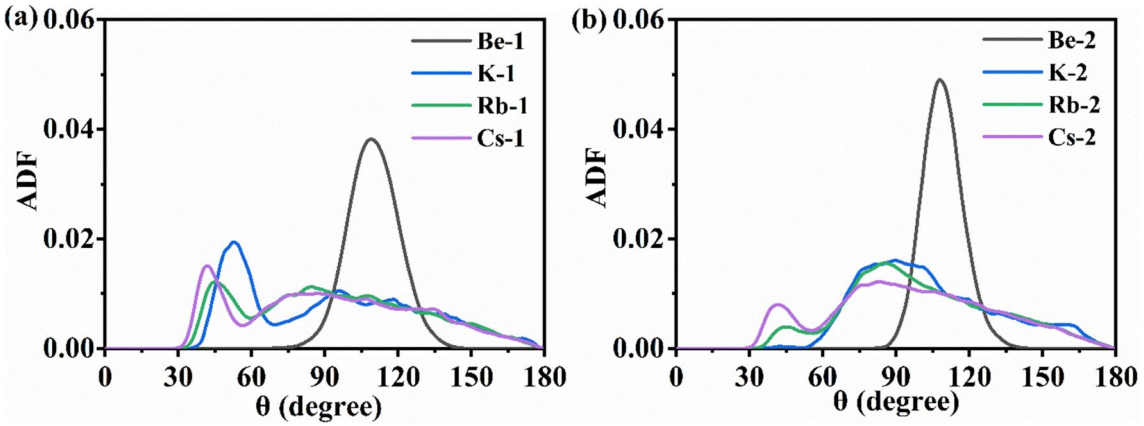

Fig. 9 ADFs of F-Be-F, F-K-F, F-Rb-F, and F-Cs-F in **a** Mixture 1 and **b** Mixture 2. (Color figure online)

Mixture 1, the diffusion coefficients of Be^{2+}, K^+, Rb^+, Cs^+, and F^- decrease to 2.55×10^{-5}, 3.15×10^{-5}, 4.02×10^{-5}, 3.23×10^{-5}, and 3.87×10^{-5} cm^2/s, respectively. Reflecting on the structural characteristics of the two systems, the binding strength between the same ion pair in Mixture 2 is stronger than that in Mixture 1, but the interactions between Be^{2+} and F^- significantly influence the overall stability of the system. Because the concentration of Be^{2+} in Mixture 1 is considerably higher than that in Mixture 2, it is more likely to form larger clusters between Be^{2+} and F^-. This can obviously reduce the diffusion coefficients of all ions in Mixture 1, especially Be^{2+} and F^-.

5 Conclusion

The binary ($KF-BeF_2$, $RbF-BeF_2$, $CsF-BeF_2$, KF-CsF, and RbF-CsF), ternary (BeF_2-KF-RbF, BeF_2-CsF-KF, BeF_2-CsF-RbF, and CsF-KF-RbF), and quaternary KF-RbF-CsF-BeF_2 systems were thermodynamically calculated using the CALPHAD technique. Furthermore, the RDFs, CNs, ADFs, and diffusion coefficients of the quaternary KF-RbF-CsF-BeF_2 system were calculated using AIMD. The main contributions of this work are as follows:

(1) A set of self-consistent and reliable thermodynamic databases for the $KF-BeF_2$, $RbF-BeF_2$, $CsF-BeF_2$, KF-CsF, and RbF-CsF systems was established.
(2) The liquidus projections and invariant points of BeF_2-KF-RbF, BeF_2-CsF-KF, BeF_2-CsF-RbF, and CsF-KF-RbF systems were obtained.
(3) The melting temperatures ($T_{m.p.} \leq 450$ °C) for quaternary KF-RbF-CsF-BeF_2 systems with different compositions were obtained.
(4) The interaction strength between cations and anions in the system followed the order Be-F > K-F > Rb-F > Cs-F. The CNs of all cations were determined.
(5) A high Be^{2+} concentration can reduce the diffusion coefficients of the ions, especially Be^{2+} and F^-.

The present study is the first of its type, to the best of our knowledge, and the results show that the quaternary KF-RbF-CsF-BeF_2 system with the proportion 3.50–28.92–21.78–45.80 mol% or 1.80–35.42–52.40–10.38 mol% is one of the most promising candidate coolants for MSRs in terms of thermodynamics (i.e., $T_{m.p.} \leq 450$ °C with appropriate viscosity) and kinetics (i.e., suitable local structure and diffusion coefficient). This work not only drastically enriches the databases of molten salts, but also provides direct guidelines for screening and optimizing molten salts in the nuclear energy field.

Author contributions All authors contributed to the study conception and design. Material preparation, data collection and analysis were performed by Hui-qin Yin, Lin-Bin Jiang, Xu-Chun Wu, Biao-Hu, Yang Wang and Wen-Guan Liu. The first draft of the manuscript was written by Hui-Qin Yin and all authors commented on previous versions of the manuscript. All authors read and approved the final manuscript.

Data availability The data that support the findings of this study are openly available in Science Data Bank at https://cstr.cn/31253.11.sciencedb.j00186.00731 and https://doi.org/10.57760/sciencedb.j00186.00731.

Declarations

Conflict of interest The authors declare that they have no competing interests.

References

1. M.L. Tan, G.F. Zhu, Z.D. Zhang et al., Burnup optimization of once-through molten salt reactors using enriched uranium and thorium. Nucl. Sci. Tech. **33**, 5 (2022). https://doi.org/10.1007/s41365-022-00995-2
2. J. Serp, M. Allibert, O. Beneš et al., The molten salt reactor (MSR) in generation IV: Overview and perspectives. Prog. Nucl. Energy. Nucl. Energy **77**, 308–319 (2014). https://doi.org/10.1016/j.pnucene.2014.02.014
3. Q. Liu, H. Sun, H. Yin et al., Corrosion behaviour of 316H stainless steel in molten FLiNaK eutectic salt containing graphite particles. Corros. Sci.. Sci. **160**, 108174 (2019). https://doi.org/10.1016/j.corsci.2019.108174
4. A technology roadmap for generation IV nuclear energy systems. Nuclear Energy Research Advisory Committee and the Generation IV International Forum, US., (2002). https://doi.org/10.2172/859029
5. M.W. Rosenthal, P.R. Kasten, R.B. Briggs, Molten salt reactors-history, status, and potential. Nucl. Appl. Technol. **8**, 107–117 (1970). https://doi.org/10.13182/NT70-A28619
6. B. Wang, X. Wang, A neutronics-thermal coupling-based rapid assessment method for molten salt reactor fuel draining system. Appl. Therm. Eng. **270**, 126169 (2025). https://doi.org/10.1016/j.applthermaleng
7. X. Ge, Y. Jiang, X. Yu et al., Preparation and characterization of graphene-nanosheet-reinforced Ni-17Mo alloy composites for advanced nuclear reactor applications. Materials **18**, 1061 (2025). https://doi.org/10.3390/ma18051061
8. H. Yu, G. Zhu, Y. Zou et al., Neutron/gamma radial shielding design of main vessel in a small modular molten salt reactor. J. Nucl. Eng. **4**, 213 (2023). https://doi.org/10.3390/jne4010017
9. J. Magnusson, M. Memmott, T. Munro, Review of thermophysical property methods applied to fueled and un-fueled molten salts. Ann. Nucl. Energy **146**, 107608 (2020). https://doi.org/10.1016/j.anucene.2020.107608
10. V. Khokhlov, V. Ignatiev, V. Afonichkin, Evaluating physical properties of molten salt reactor fluoride mixtures. J. Fluor. Chem. **130**, 30–37 (2009). https://doi.org/10.1016/j.jfluchem.2008.07.018
11. O. Beneš, R.J.M. Konings, Thermodynamic properties and phase diagrams of fluoride salts for nuclear applications. J. Fluor. Chem. **130**, 22–29 (2009). https://doi.org/10.1016/j.jfluchem.2008.07.014
12. H. Yin, P. Zhang, X. An et al., The effect of corrosion product CrF_3 on thermo-physical properties of FLiNaK. J. Nucl. Sci.

Technol. **53**, 61–68 (2016). https://doi.org/10.1080/00223131.2015.1026859
13. C. Liao, L. Que, Z. Fu et al., Research status of electrolytic preparation of rare earth metals and alloys in fluoride molten salt system: a mini review of China. Metals **14**, 407 (2024). https://doi.org/10.3390/met14040407
14. O. Beneš, R.J.M. Koings, Thermodynamic study of LiF–BeF_2–ZrF_4–UF_4 system. J. Alloys Compd. **452**, 110–115 (2008). https://doi.org/10.1016/j.jallcom.2007.01.184
15. R.Y. Zakirov, V.V. Ignatiev, Fuel cycle of the LiF–BeF_2 molten salt actinide burner reactor. Phys. At. Nucl.Nucl. **86**, 1894–1901 (2023). https://doi.org/10.1134/S1063778823080276
16. A. Romero-Serrano, M. Hallen-Lopez, B. Zeifert et al., Thermodynamic analysis of LiF–BeF_2 and KF–BeF_2 melts by a structural model. J. Fluor. Chem. **130**, 336–340 (2009). https://doi.org/10.1016/j.jfluchem.2008.12.008
17. C. Griffard, S.G. Penoncello, J.C. Crepeau, Use of the soft-sphere equation of state to predict the thermodynamic properties of the molten salt mixtures LiF–BeF_2, NaF–BeF_2, and KF–BeF_2. Prog. Nucl. Energy **68**, 188–199 (2013). https://doi.org/10.1016/j.pnucene.2013.06.008
18. X.M. Yang, H.J. Liu, B.C. Chen et al., Corrosion behavior of GH3535 alloy in molten LiF–BeF_2 salt. Corros. Sci.. Sci. **199**, 110168 (2022). https://doi.org/10.1016/j.corsci.2022.110168
19. P.N. Haubenreich, J. Engel, Experience with the molten salt reactor experiment. Nucl. Appl. Technol. **8**, 118–137 (1970). https://doi.org/10.13182/NT8-2-118
20. D.M. Roy, R. Roy, E.F. Osborn, Fluoride model systems: IV, the systems LiF-BeF_2 and PbF_2-BeF_2. J. Am. Ceram. Soc. **37**, 300–305 (1954). https://doi.org/10.1111/j.1151-2916.1954.tb14042.x
21. R.E. Thoma, Phase Diagrams of Nuclear Reactor Materials. ORNL report No. 2548, Oak Ridge, Tennessee, US., (1959)
22. K.A. Romberger, J. Braustein, R.E. Thoma, New electrochemical measurements of the liquidus in the lithium fluoride-beryllium fluoride system. congruency of lithium beryllium fluoride (Li_2BeF_4). J. Phys. Chem. **76**, 1154–1159 (1972). https://doi.org/10.1021/j100652a012
23. B.F. Hitch, C.F. Baes Jr., Electromotive force study of molten lithium fluoride-beryllium fluoride solutions. Inorg. Chem. **8**, 201–207 (1969). https://doi.org/10.1021/ic50072a004
24. J.L. Holm, O.J. Kleppa, Enthalpies of mixing in liquid beryllium fluoride-alkali fluoride mixtures. Inorg. Chem. **8**, 207–212 (1969). https://doi.org/10.1021/ic50072a005
25. J.P.M. Van Der Meer, R.J.M. Konings, M.H.G. Jacobs et al., A miscibility gap in LiF–BeF_2 and LiF–BeF2–ThF4. J. Nucl. Mater. Nucl. Mater. **344**, 94–99 (2005). https://doi.org/10.1016/j.jnucmat.2005.04.023
26. S. Fukada, A. Nakamura, Estimation of melting points for some binary and tertiary fluoride molten salts. Fusion Sci. Technol. **66**, 322–336 (2014). https://doi.org/10.13182/FST13-694
27. W.R. Grimes, Reactor chemistry division annual progress report for period ending December 31, 1965, ORNL report No. 3913. Oak Ridge, Tennessee, US., (1966). https://doi.org/10.2172/4547015
28. S. Cantor, W. Ward, C. Moynihan, Viscosity and density in molten BeF_2–LiF solutions. J. Chem. Phys. **50**, 2874–2879 (1969). https://doi.org/10.1063/1.1671478
29. M.W. Rosenthal, P.B. Briggs., P.R. Kasten, Molten-salt reactor program semiannual progress report, ORNL report No. 4449, Oak Ridge, Tennessee, US., (1970)
30. K.A Tasidou, J. Magnusson, T. Munro et al., Reference correlations for the viscosity of molten LiF-NaF-KF, LiF-BeF_2, and Li_2CO_3-Na_2CO_3-K_2CO_3. J. Phys. Chem. Ref. Data **48**, 043102 (2019). https://doi.org/10.1063/1.5131349
31. O.Y. Tkacheva, A.V. Rudenko, A.A. Kataev et al., The viscosity of molten salts based on the LiF–BeF_2 system. Russ. J. Non-Ferrous Met. **63**, 276–283 (2022). https://doi.org/10.3103/S1067821222030117
32. M.A. Greenbaum, J.N. Foster, M.L. Arin et al., The thermodynamic and physical properties of beryllium compounds. I. enthalpy and entropy of vaporization of beryllium fluoride. J. Phys. Chem. **67**, 36–40 (1963). https://doi.org/10.1021/j10079 5a009
33. M. Salanne, C. Simon, P. Turq et al., A first-principles description of liquid BeF_2 and its mixtures with LiF: 2. network formation in LiF−BeF_2. J. Phys. Chem. B **110**, 11461–11467 (2006). https://doi.org/10.1021/jp061002u
34. B.S. Jabes, M. Agarwal, C. Chakravarty, Structure and transport properties of LiF–BeF_2 mixtures: comparison of rigid and polarizable ion potentials. J. Chem. Sci. **124**, 261–269 (2012). https://doi.org/10.1007/s12039-012-0225-5
35. A.L. Smith, E. Capelli, R.J.M. Konings et al., A new approach for coupled modelling of the structural and thermo-physical properties of molten salts. Case of a polymeric liquid LiF-BeF_2. J. Mol. Liq. **299**, 112165 (2020). https://doi.org/10.1016/j.molliq.2019.112165
36. Y.J. Li, X.Y. Liu, B.Z. Wang et al., Raman and theoretical studies on structural evolution of Li_2BeF_4 and binary LiF-BeF_2 melts. J. Mol. Liq. **325**, 115208 (2021). https://doi.org/10.1016/j.molliq.2020.115208
37. D.M. Roy, R. Roy, E.F. Osborn, Fluoride model systems: III, the system NaF–BeF_2 and the polymorphism of Na_2BeF_4 and BeF_2. J. Am. Ceram. **36**, 185–190 (1953). https://doi.org/10.1111/j.1151-2916.1953.tb12864.x
38. S. Wu, X. Li, P. Zhang et al., Thermodynamic evaluation of NaF-MFn(M=Be, U, Th) systems for molten salt reactor. Chem. Res. Chin. Univ. **34**, 457–463 (2018). https://doi.org/10.1007/s40242-018-7398-5
39. G.J. Janz, G. Gardner, U. Krebs et al., Molten salts: volume 4, Part 1, fluorides and mixtures electrical conductance, density, viscosity, and surface tension data. J. Phys. Chem. Ref. Data **3**, 1–115 (1974)
40. K.A. Sense, R.W. Stone, Vapor pressures and molecular composition of vapors of the sodium fluoride-beryllium fluoride system. J. Phys. Chem. **62**, 453–457 (1958). https://doi.org/10.1021/j150562a020
41. G.T. Fukuda, P.F. Peterson, D.R. Olander et al., Thermodynamics of the LiF–NaF–BeF_2 system at high temperatures. Fluid Phase Equilib. **255**, 1–10 (2007). https://doi.org/10.1016/j.fluid.2007.01.041
42. J.C. Sun, H.L. Huang, H.Y. Wu et al., HT-NMR studies of the Be–F coordination structure in FNaBe and FLiBe mixed salts. JACS Au **4**, 2211–2219 (2024). https://doi.org/10.1021/jacsau.4c00177
43. M.M. Liu, X.J. Li, T.R. Xu et al., Mapping relationships between cation-F bonds and the heat capacity, thermal conductivity, viscosity of molten NaF-BeF_2. J. Mol. Liq. **354**, 118915 (2022)
44. M.P. Borzenkova, Yu.P. Simanov, V.I. Chernykh et al., Thermal and X-ray analysis of the KF-BeF_2 system. Zbur. Neorg. Kbirn. **1**, 2071–2082 (1956)
45. A. V. Novoselova, Y. M. K., M. P. Borzenkova, KF-BeF_2 system. Zh. Neorg. Khim. **9**, 2042 (1964)
46. R.G. Grebenshchikov, Investigation of the phase diagram of the RbF-BeF_2 system and of its relationship to the BaO-SiO system. Dokl. Akad. Nauk SSSR **114**, 316–319 (1957)
47. O.N. Breusov, A.V. Novoselova, Y.P. Simanov, Thermal and X-ray phase analysis of the system CsF-BeF_2 and its interrelationship with MeF and BeF2 systems. Dokl. Akad. Nauk SSSR **118**, 935–937 (1958)
48. K. Baral, S. San, R. Sakidja et al., Temperature-dependent properties of molten Li2BeF4 salt using Ab initio molecular dynamics.

ACS Omega **6**, 19822–19835 (2021). https://doi.org/10.1021/acsomega.1c02528
49. J.X. Dai, H. Han, Q.N. Li et al., First-principle investigation of the structure and vibrational spectra of the local structures in LiF–BeF_2 molten salts. J. Mol. Liq. **213**, 17–22 (2016). https://doi.org/10.1016/j.molliq.2015.10.053
50. X.J. Li, T.R. Xu, M.M. Liu et al., Diffusion behaviors of HF in molten LiF-BeF_2 and LiF-NaF-KF eutectics studied by FPMD simulations and electrochemical techniques. J. Nucl. Mater.Nucl. Mater. **572**, 154031 (2022). https://doi.org/10.1016/j.jnucmat.2022.154031
51. X.J. Li, Influence of ZrF4 additive on the local structures and thermophysical properties of molten NaF-BeF_2. J. Mol. Liq. **393**, 123681 (2024). https://doi.org/10.1016/j.molliq.2023.123681
52. H. Rezvantalab, G. Drazer, S. Shojaei-Zadeh, Molecular simulation of translational and rotational diffusion of Janus nanoparticles at liquid interfaces. J. Chem. Phys. **142**, 014701 (2015). https://doi.org/10.1063/1.4904549
53. R.G. Samuseva, V.E. Plyushchev, System CsF-KF and Cs-RbF. Zh. Neorg. Khim. **10**, 1270–1272 (1965)
54. O. Benes, P. Zeller, M. Salanne et al., Density functional theory, molecular dynamics, and differential scanning calorimetry study of the RbF-CsF phase diagram. J. Chem. Phys. **13**, 134716 (2009). https://doi.org/10.1063/1.3097550
55. J. Sangster, A.D. Pelton, Phase diagrams and thermodynamic properties of the 70 binary alkali halide systems having common ions. J. Phys. Chem. Ref. Data **16**, 509–561 (1987). https://doi.org/10.1063/1.555803
56. H.Q. Yin, S. Wu, X.L. Wang et al., Thermodynamic description for the NaF-KF-RbF-ZnF_2 system. J. Fluor. Chem. **217**, 90–96 (2019). https://doi.org/10.1016/j.jfluchem.2018.09.008
57. H.Q. Yin, X.M. Wu, C.J. Ling et al., Thermodynamic optimization of the constitutive binaries of the LiCl/RbCl/$CaCl_2$-NaCl-UCl_3-$PuCl_3$ systems. Calphad **77**, 102427 (2022). https://doi.org/10.1016/j.calphad.2022.102427
58. T.R. Xu, X.J. Li, Y. Wang et al., Development of deep potentials of molten $MgCl_2$–NaCl and $MgCl_2$–KCl salts driven by machine learning. ACS Appl. Mater. **15**, 14184–14195 (2023). https://doi.org/10.1021/acsami.2c19272
59. S.Y. Lin, X.J. Li, L.B. Jiang et al., First-principles study on the diffusion behavior of Cs and I in Cr coating. Nucl. Sci. Tech. **35**, 100 (2024). https://doi.org/10.1007/s41365-024-01460-y
60. G. Kresse, J. Furthmüller, Efficiency of ab-initio total energy calculations for metals and semiconductors using a plane-wave basis set. Comput. Mater. Sci. **6**, 15–50 (1996). https://doi.org/10.1016/0927-0256(96)00008-0
61. G. Kresse, J. Furthmüller, Efficient iterative schemes for ab initio total-energy calculations using a plane-wave basis set. Phys. Rev. B **54**, 11169–11186 (1996). https://doi.org/10.1103/PhysRevB.54.11169
62. B.L. Zhang, W.G. Liu, M.H. Tu et al., Adhesion property of AlCrNbSiTi high-entropy alloy coating on zirconium: experimental and theoretical studies. Nucl. Sci. Tech. **35**, 141 (2024). https://doi.org/10.1007/s41365-024-01508-z
63. J.P. Perdew, J.A. Chevary, S.H. Vosko et al., Atoms, molecules, solids, and surfaces: applications of the generalized gradient approximation for exchange and correlation. Phys. Rev. B Condens. MatterCondens. Matter **46**, 6671–6687 (1992). https://doi.org/10.1103/PhysRevB.46.6671
64. B. Perdew, Ernzerhof, generalized gradient approximation made simple. Phys. Rev. Lett. **77**, 3865–3868 (1996). https://doi.org/10.1103/PhysRevLett.77.3865
65. P.E. Blochl, Projector augmented-wave method. Phys. Rev. B Condens. MatterCondens. Matter **50**, 17953–17979 (1994). https://doi.org/10.1103/PhysRevB.50.17953
66. J.D. Pack, H.J. Monkhorst, Special points for Brillouin zone integrations'a reply. Phys. Rev. B **16**, 1748–1749 (1977). https://doi.org/10.1103/PhysRevB.16.1748
67. M. Parrinello, A. Rahman, Crystal structure and pair potentials: a molecular-dynamics study. Phys. Rev. Lett. **45**, 1196–1199 (1980). https://doi.org/10.1103/PhysRevLett.45.1196
68. D.J. Evans, Computer "experiment" for nonlinear thermodynamics of Couette flow. J. Chem. Phys. **78**, 3297–3302 (1983). https://doi.org/10.1063/1.445195
69. W.G. Hoover, Canonical dynamics: equilibrium phase-space distributions. Phys. Rev A. Gen. Phys. **31**, 1695–1697 (1985). https://doi.org/10.1103/PhysRevA.31.1695
70. S. Nose, A unified formulation of the constant temperature molecular dynamics methods. J. Chem. Phys. **81**, 511–519 (1984). https://doi.org/10.1063/1.447334
71. L.B. Jiang, J. Qiu, S.Y. Lin et al., Chemical states of corrosion products in liquid lead from ab initio molecular dynamics. J. Nucl. Mater.Nucl. Mater. **599**, 155237 (2024). https://doi.org/10.1016/j.jnucmat.2024.155237
72. Y. Xie, M. Bu, G.M. Zou et al., Molecular dynamics simulations of $CaCl_2$–NaCl molten salt based on the machine learning potentials. Sol. Energy Mater. Sol. Cells **254**, 112275 (2023). https://doi.org/10.1016/j.solmat.2023.112275